Evolution and spatio-temporal characteristics of slope erosion due to rainfall in Southwest China

Ganglie Yuan[1] · Ailan Che[1]

Abstract

Soil in rainy and moist regions is influenced by heavy rainfall, which results in erosion from exposed slopes; local collapse and landslide may occur with the evolution of slope erosion. To determine the time–space effect of heavy rainfall on a slope, an in situ model test of a granite slope that was completely decomposed due to rainfall was conducted. The resistivity profile and surface shape parameters of the slope under continuous rainfall were monitored through electrical measurements and three-dimensional laser scanning. Infiltration and slope erosion evolution were analyzed based on the relationships between erosion rate and resistivity. With an increase in rainfall duration, a creep-type growth trend was observed for rill density on the slope surface with rill density change rates of approximately 0.6%/h, 0.1%/h, and 0.7%/h. A gradual decreasing trend of rill density was observed from the bottom to the top of the slope, and the decrease was approximately three times. When the rainfall duration was 12 h, a step-type growth trend for erosion rate was observed from 8.0–11.3 to 21.8–38.8%, i.e., an increase of approximately three times, indicating a transition from low-speed to high-speed growth in erosion. A gradual decreasing trend erosion rate was observed from the shallow to deep part of the slope; the average growth rates were 33.0%, 15.2%, and 4.9% when the rainfall duration was 16 h.

Keywords Slope erosion · Rainfall · Model test · Evolution process · Spatio-temporal characteristics

Introduction

A large number of exposed slopes are formed due to engineering construction. These slopes are affected by the external environmental factors, such as heavy rainfall. In particular, slopes with special soil, such as granite and loess, in rainy and moist regions, decompose completely; thus, they are easily dispersed and have poor water stability (Biswas and Roy 2018). Under the influence of rainfall, large amounts of soil are lost, leading to soil erosion, vegetation destruction, and other ecological and environmental problems (Comino et al. 2017). For example, during excavation of the Congo (Brazzaville) No. 1 Highway Noire to Brazzaville, the vegetation cover was destroyed, and a large area of secondary bare land was produced by soil erosion due to rainfall (Liu et al. 2014). Destruction of the ecological environment aggravates slope erosion, decreasing soil strength through a change in soil structure (Chen et al. 2004). Local collapse and landslide occur with the evolution of slope erosion (Wen and Deng 2020; Yu et al. 2019; Hicher 2013). For example, the slope of the Lei-Yi Highway in Southwest China was deformed and destroyed due to long-term rainfall and soil erosion. The security and durability of highways in northern and northeastern Morocco have been compromised due to rainfall erosion that generated significant soil losses (Chehlafi et al. 2019).

Several studies have demonstrated temporal and spatial evolution characteristics of slope erosion (Cui et al. 2019; Crosta and Prisco 1999). Slope erosion is a comprehensive action of gravity, cohesive force between particles, buoyancy, drag force, upward force, and seepage pressure (Forster and Meyer 1972). In the process of slope erosion, particles with less anti-erosion ability move, accumulate at the bottom of the slope, and migrate along the slope depth as a result of runoff and infiltration, indicating that the survival chances of vegetation decrease due to slope erosion

✉ Ailan Che
  alche@sjtu.edu.cn

1 Shanghai Key Laboratory for Digital Maintenance
   of Buildings and Infrastructure, School of Naval
   Architecture, Ocean and Civil Engineering, Shanghai
   Jiao Tong University, 800 Dongchuan-Road, Shanghai 200240,
   China

up to a certain depth (Wu et al. 2014). The internal structure of the soil is destroyed during slope erosion; soil properties change due to changes in the internal soil structure. The mechanical properties of granular material are influenced by erosion parameters (Hama et al. 2017). A progressive decrease in critical shear stress and soil infiltrability results from the structure degradation of soil surface due to rainfall (Léonard and Richard 2004). Soil porosity and pore-water pressure increase with an advancing water front and due to internal erosion (Zhang et al. 2019). The spatio-temporal characteristics of slope erosion produce spatial and temporal changes in soil strength.

The Mo-Lin Highway, Yunnan Province, has many completely decomposed granite cutting slopes formed by excavation, which have led to soil erosion, local collapse, and slope instability. The spatio-temporal characteristics of soil erosion on the slope vary with rainfall, as shown in Fig. 1. The rill rate and depth in the upper region of the slope are greater than that in the lower region, as shown in Fig. 1e and f. Sediment effluents are observed on the slope, and coarse particles mix with the effluents in the lower area, as shown in Fig. 1g and h. Vegetation cannot grow easily on the slope under the influence of soil erosion, as shown in Fig. 1i and j. The effect of soil erosion is intensified on an unprotected slope. Thus, determining the temporal and spatial evolution mechanism of slope erosion with rainfall and evaluating the degree of slope erosion in different regions of a slope are of great engineering significance. Due to the migration of soil particles along the slope and depth with rainfall, the spatial distribution of soil erosion changes. To predict slope erosion and stability, it is important to understand the evolution process of slope erosion and the temporal and spatial characteristics of slope erosion in each stage.

Researchers have conducted studies on the temporal and spatial evolution of soil erosion parameters and methods of testing the soil erosion process (Biali et al. 2014). With changes in erosion degree, the hydrodynamic parameters of the slope surface, such as velocity, Reynolds number, and particle migration and movement, exhibit spatio-temporal evolution (Grigor'ev et al. 2008). Existing test methods used for examining the soil erosion process during rainfall are based mainly on sensor monitoring, laser-scanned topography, and soil mechanics experiments (Wang and Lai 2018). In soil mechanics experiments, a laboratory flume is to simulate rainfall and conduct quantitative soil erosion analyses. Erosion of the bottom of a fine-grained silty loess slope evolves rapidly and produces landslides eventually (Acharya et al. 2011). Sensors (moisture content and pore pressure) are also used to monitor temporal and spatial changes in moisture content and pore pressure in the soil erosion process (Kim and Lee 2010). However, these methods are complex, and real-time multidimensional erosion testing of slopes is not possible during rainfall. Temporal and spatial evolution of a

slope surface has been studied using a slope surface morphological parameter. However, there has been a lack of research on evolution along the slope depth, which is important in determining the degree of erosion and in stability analysis of the entire slope.

Electrical parameters of soil are sensitive to moisture content and structure. Electrical measurement methods are geophysical exploration techniques used to identify different types of useful deposits and geological structures and to solve geological problems (Cano-Paoli et al. 2019). As electrical measurements are highly efficient, they can be applied in many fields. Pizer et al. (1987) developed a test method for determining the durability-related properties of decades-old cement composites through electrical resistivity measurements. Ahmad (2018) detected the depth of underground cracks through electrical resistivity tomography. In the evaluation of slope erosion, the internal structure of soil plays a major role in slope erosion due to rainfall, whereas runoff and infiltration are transient. The relationship between soil resistivity and structure can be established using CT and mechanical experimental tests (Fang et al. 2012). Field electrical measurements are therefore significant for the evaluation of slope erosion with rainfall (Karim and Tucker-Kulesza 2018).

To clarify the evolution process and spatio-temporal characteristics of slope erosion due to rainfall, a completely decomposed granite slope model of a highway under construction was selected. A rainfall experiment was set up with electrical measurements and three-dimensional (3D) laser scanning. Using the temporal and spatial variations in the electrical and erosion parameters under different precipitations, the evolution laws of slope erosion due to rainfall were analyzed, and the spatio-temporal characteristics of slope erosion were determined. Accordingly, the erosion degree was determined, and the stability of field slopes was analyzed.

In situ rainfall model test

Completely decomposed granite is a special material that is soft and can easily disperse in water; it has a loose structure, poor water stability, and small cohesive force. Thus, the soil erosion of a completely decomposed granite slope becomes severe with rainfall. An in situ model test was designed in this study; the soil erosion process of a granite slope that was completely decomposed due to rainfall was evaluated through electrical measurements and 3D laser scanning.

Study area and slope

Completely decomposed granite is distributed in southeastern and southwestern China. There are 67 highways under
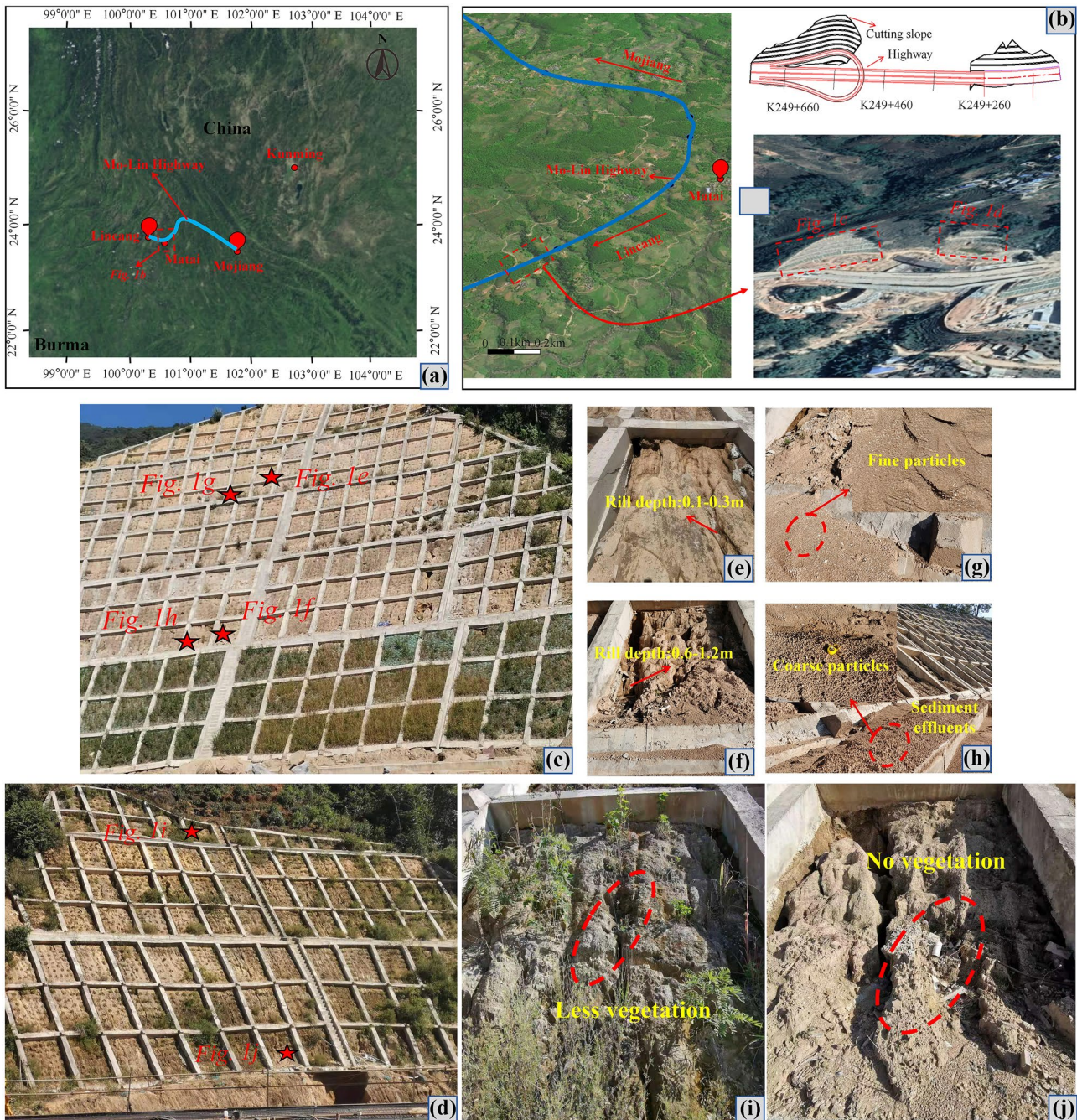
Fig. 1 Investigation of soil erosion with rainfall along Mo-Lin Highway. **a** Map showing highway construction in Yunnan Province; **b** map showing cutting slope with high soil erosion; **c** investigation area 1 with high, steep slope; **d** investigation area 2 with low slope; **e** development of cracks in upper region of slope; **f** development of cracks in lower region of slope; **g** sediment effluents in upper region of slope; **h** sediment effluents in lower region of slope; **i** vegetation coverage in upper region of slope; **j** vegetation coverage in lower region of slope

construction in Yunnan Province in southwestern China, with a total mileage of 4000 km. The model test design is based on the Mo-Lin Highway (under construction) in Yunnan Province in southern China, as shown in Fig. 2. Granite and sand are widely distributed in this area. Rainfall in this area is heavy, concentrated, and continuous. The annual average precipitation is 1112.0–1964.4 mm, and the annual average relative humidity is 70–80%.

The soil in the test region is completely decomposed granite, as shown in Fig. 3. The natural density is 1.96 g/cm^3. The allowable bearing capacity is 280 kPa, and the standard soil friction at the side of the bored pile is 90 kPa.

Fig. 2 Background of highway under construction and geological conditions
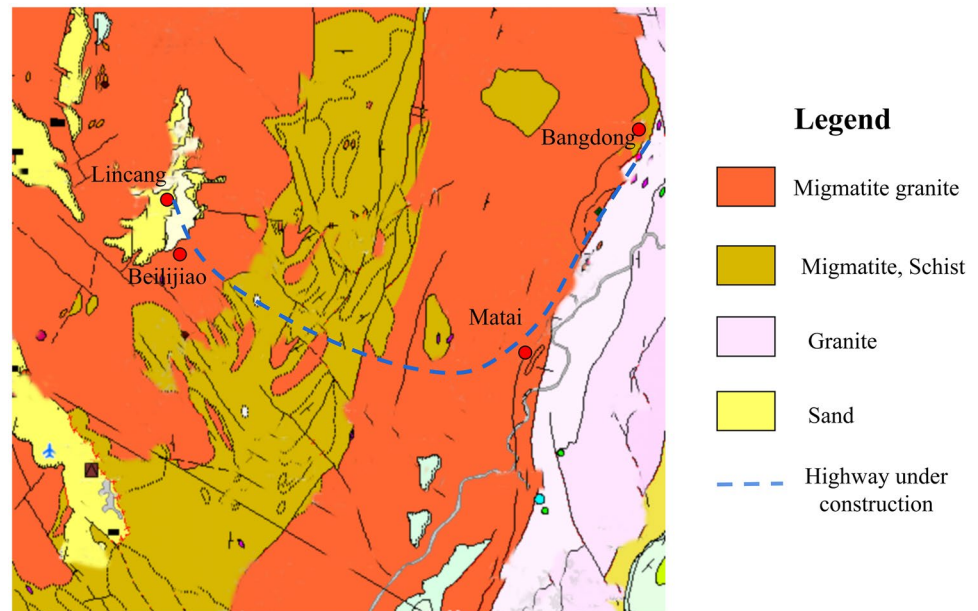
The clay mineral content in the soil is 26.36%. In addition to clay minerals, albite and quartz are primary soil components, with a content of approximately 25%.

For the experiment, a section of the subgrade slope was selected as the test object, and the slope angle was set to 38°, as shown in Fig. 3. An area of 6×6 m^2 (length × width) in the center was selected as the test area. The surface of the slope test area was leveled; two trenches were set in the lower part of the test area to facilitate collection of surface runoff and sediment. Fixed frames were set up in the upper and surrounding areas to construct the rainfall system.

The rainfall system included a water supply pressurization system, rainfall sprinkler, and flow control system. The water supply pressurization system consisted of a flume, pump, and water pipes. The water in the flume was pumped to the designated location using water pipes and pumps. Four pipes were arranged in the test area, with a spacing of 1.5 m; each pipe was set with four nozzles spaced 1.5 m apart. Water was sprayed through the nozzles to simulate rainfall. The scour effluent was collected through a catchment trench. The flow was controlled and recorded by the flow control system.

Monitoring methods

Methods to monitor soil erosion in rainfall were designed, including electrical measurements and 3D laser scanning, as shown in Figs. 3 and 4. The electrical measurement system consisted of an electrical instrument host, battery, booster, electrodes, and cables. The electrodes were arranged on the surface of the slope. Electrical signals were transmitted by the connected cables, and the data were recorded by the electrical instrument host. The 3D laser scanning system consisted of a tripod, scanning host, and target marks. The system was used for real-time monitoring of the slope surface state. Based on the rill density statistics obtained from the 3D laser scanning test, the soil erosion of the slope was quantitatively calculated using the volumetric method. Sediment effluents were collected by the catchment trench at the bottom of the slope. The sediment mass was measured by the drying method, and the results obtained using the volumetric method were verified.

Soil materials exhibit different conductivities, magnetic permeabilities, and electrochemical properties (Ayodele et al. 2017). The electrical conductivity and strength of soil change with the loss of fine grains and changes in soil structure due to rainfall. Theoretical relationships suggest that the soil structure can be measured and evaluated through electrical measurements (Cai et al. 2015).

The ground was assumed to be a half-space. A steady current field was established in the ground by the power supplied using a pair of conductive electrodes A and B, with a distance of L_{AB} between them and a direct current of intensity I (measured using a galvanometer), as shown in Fig. 5. The potential difference ΔU between the other two conductive and nonpolarized electrodes, M and N, was measured. With an increase in electrode spacing L_{AB}, the depth of the measuring points increased. The positions and distances of the electrodes were changed to determine the resistivity distribution of the soil at different depths. The value of ρ_s at the measuring point (the midpoint between M and N) for each layer (the electrode spacing L_{AB} remained unchanged) was calculated using the following equation:

Fig. 3 Construction of slope model and selection of test area to simulate rainfall
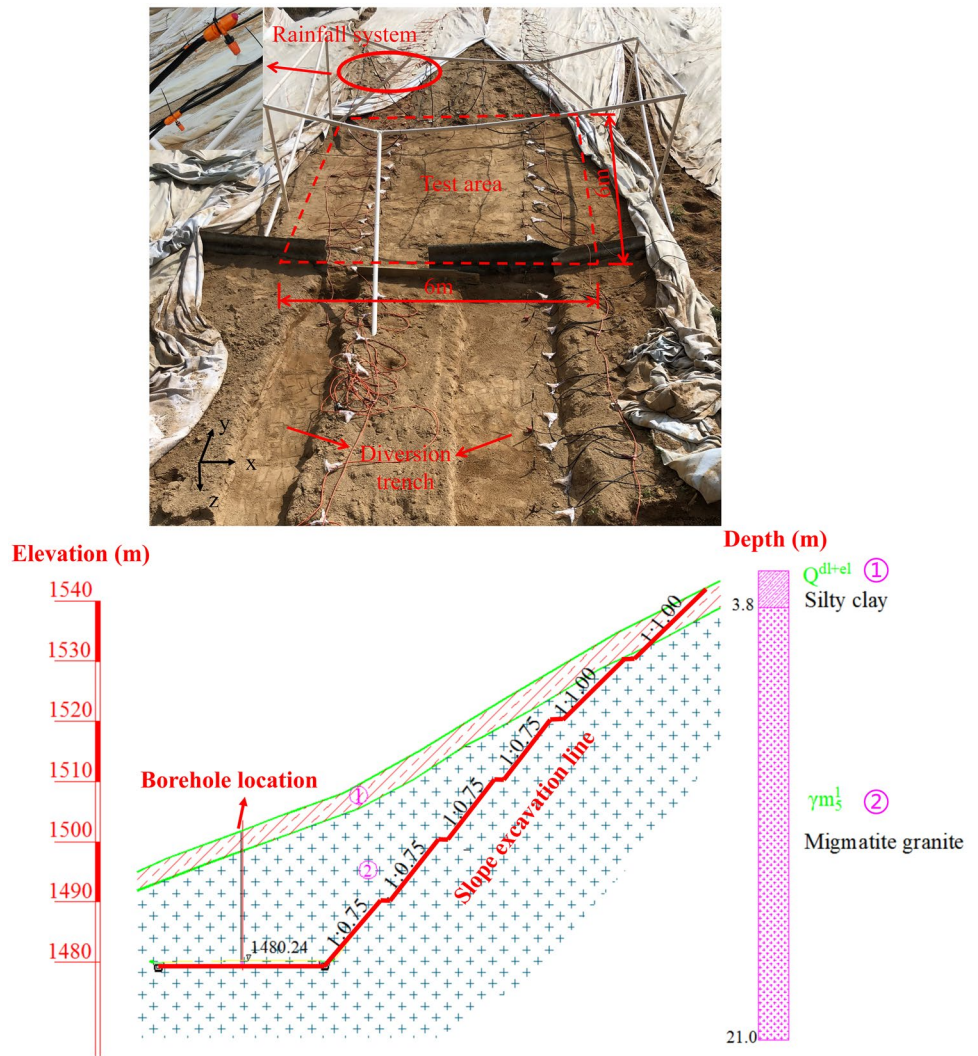
$$\rho_s = K \cdot \frac{\Delta U}{I} \tag{1}$$

where ρ_s is the apparent resistivity. When the electrodes were moved forward, the apparent resistivity of the soil was determined by measuring the value of ρ_s point by point. For a nonhomogeneous isotropic medium with resistivity, $\rho_s = \rho_1, \rho_2, \ldots, \rho_n$. When the electrode spacing L_{AB} was increased, the apparent resistivity of the soil at different depths was determined in the same way. When the soil resistivity changed as a result of soil erosion, the resistivity change in each layer $\Delta\rho$ was measured through electrical measurements. K is the electrode arrangement coefficient, which is related to the relative positions and spacings of electrodes A, B, M, and N. For a given electrode arrangement, K is constant (Masrur et al. 2019).

Two survey lines were laid in the model test, as shown in Fig. 6. The length of the survey lines and the distance between the survey lines required to reach the detection depth were 30 m and 3.0 m, respectively. In each survey line, 60 electrodes were arranged at intervals of 0.5 m. A high-density resistivity test was conducted using the Wenner arrangement method for each survey line.

An active emission scanning light source (laser) was used for 3D laser scanning. By detecting the emitted laser echo signal, target object data can be obtained, as shown in Fig. 7. With the slope as the target, a slope image was captured when a crack was observed on the slope surface, and data at the crack for point P was measured. The reflection intensity I was collected at each point on the slope surface. By measuring the distance S, the horizontal scanning angle α, and the vertical scanning angle θ in relation to the target marks, the position coordinates of point P were obtained using the following equation:

$$\begin{cases} X = S \cos\theta \cos\alpha \\ Y = S \cos\theta \sin\alpha \\ Z = S \sin\alpha \end{cases} \tag{2}$$

Fig. 4 Monitoring methods for soil erosion with electrical measurements and 3D laser scanning
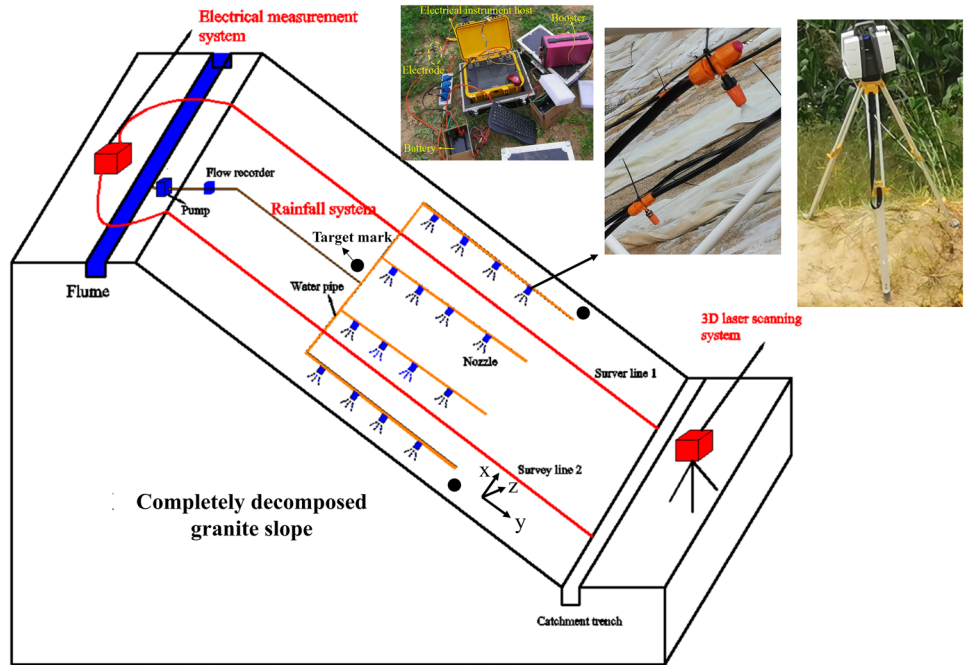
Test cases

Precipitation is a measure of cumulative rainfall, represented as the product of rainfall intensity and duration. The rainfall intensity was fixed in the test. The change in the erosion degree with different rainfall durations was analyzed by two methods. The designed rainfall intensity was 3.3 mm/h (Table 1). There were nine soil states with different rainfall durations from $t = 0$ h to $t = 16$ h. The rainstorm state was simulated for a rainfall duration of 16 h and precipitation of 53.3 mm. The rainfall duration interval between states was 2 h. During rainfall, electrical measurements were obtained,

and 3D laser scanning was performed. The initial state data for the slope were recorded. The soil resistivity was measured in real time by electrical measurements; point cloud data and reflection intensity in the slope were recorded simultaneously.

Monitoring data analysis

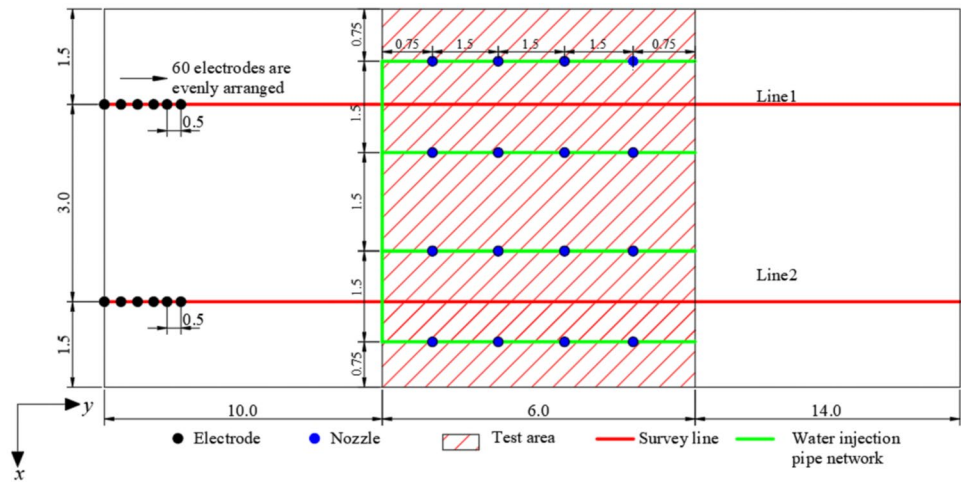### Resistivity distribution analysis in rainfall

The resistivity profiles were obtained for different states, as shown in Fig. 8. The resistivity of the slope soil ranged

Fig. 5 Principle of electrical sounding using the Wenner arrangement method
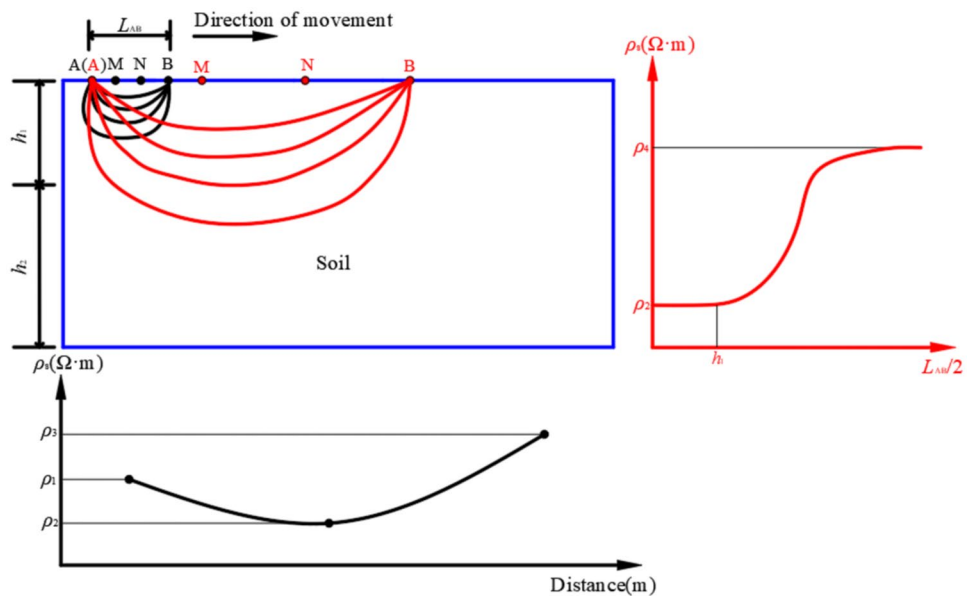
Fig. 6 Survey line layout for electrical measurements in test area (unit, m)

between 150 and 250 Ω·m, with an average value of 201 Ω·m at $t = 0$. During rainfall, the resistivity of the shallow layer of the slope changed owing to infiltration and soil erosion. A layered analysis was conducted at intervals of −0.2 m in the depth direction, and changes in resistivity were measured in each layer in each rainfall state, as shown in Fig. 9. At a depth of −0.4 m, soil erosion had little impact on the initial state ($t = 0$–12 h), whereas infiltration had a significant impact. As resistivity decreases with increasing moisture content (Kibria 2014), a decreasing trend of resistivity was observed. The resistivity at greater depths ranged from 200 to 500 Ω·m. With the disturbance caused by rainfall, the resistivity at greater depths entered a disorderly fluctuation state with a small change in the average value. With an increase in rainfall duration, the shallow surface soil reached a saturation state, and the degree of soil erosion increased. When $t = 12$ h, the soil resistivity increased due to particle composition loss. The average resistivity values from $t = 6$ h to $t = 16$ h between 0 and 0.4 m were 122 Ω·m, 122 Ω·m, 102 Ω·m, 106 Ω·m,

and 116 Ω·m. With an increase in rainfall duration, the soil at greater depths was affected by infiltration and migration of soil in a disorderly fluctuation state. The average resistivity from $t = 6$ h to $t = 16$ h at greater depths was 221 Ω·m, 229 Ω·m, 211 Ω·m, 234 Ω·m, and 233 Ω·m.

To eliminate the influence of soil type, temperature, and other factors, the growth rate of resistivity $\Delta\rho_0$ in different states, which is affected by moisture content and soil erosion, was introduced to analyze the spatio-temporal variation in resistivity during rainfall:

$$\Delta\rho_0 = \frac{\rho_n - \rho_0}{\rho_0} \tag{3}$$

where n is the number of states; $t = 2n$; ρ_n is the resistivity when $t = 2n$; and ρ_0 is the resistivity when $t = 0$. The temporal and spatial variations in resistivity were obtained from electrical measurements, as shown in Fig. 10. The resistivity at greater depths entered a state of disorderly fluctuation, and the growth rate of resistivity was positive. The icon color is the same when the resistivity growth rate is positive or zero. Similarly, profiles with a resistivity growth rate less than or equal to −80% have the same icon color. From the two survey line results, the resistivity growth rate at the beginning of the rainfall test was less than −20%. With an increase in rainfall duration, the resistivity growth rate (0– −0.2 m) decreased to −30 to −40% due to infiltration; in the lower layer (−0.2 to −0.4 m), it reached −20 to −60%. At the end of the rainfall experiment, the degree of soil erosion increased and the resistivity growth rate increased to between −20 and −40%. The change in growth rate was more prominent at the bottom of the slope than at the top of the slope.

Slope surface shape parameters analysis in rainfall

The point cloud and image data from 3D laser scanning were analyzed, and the rill distribution of the slope surface
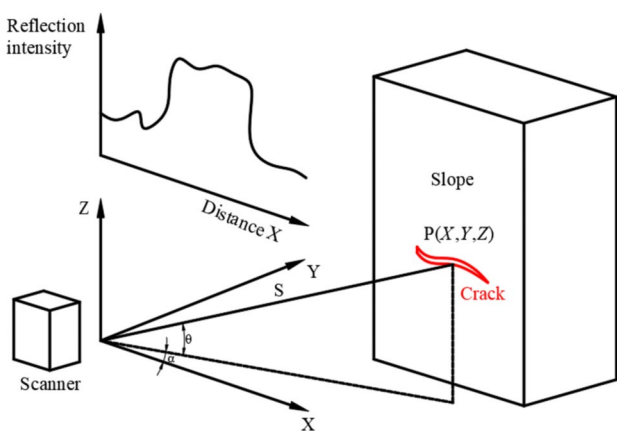
Fig. 7 Principle of slope crack monitoring using 3D laser scanning

Table 1 Test cases

Rainfall duration (h)	Rainfall intensity (mm/h)	Monitoring methods			
		Electrical measurement		3D laser scanning	
		Test status	Test content	Test status	Test content
0	0	√		√	
2	3.3	/		/	
4	3.3	/		/	
6	3.3	√		√	Point cloud data in slope, reflection intensity
8	3.3	√	Resistivity	√	
10	3.3	√		√	
12	3.3	√		√	
14	3.3	√		√	
16	3.3	√		√	

in each state was obtained, as shown in Fig. 11. The image data file was preprocessed using the K-means algorithm. Two points were selected as the initial cluster center of the gray value sample data; iterative calculations were subsequently performed to transfer the sample data to each cluster center. The error was corrected in real time to adjust the cluster center until the material segmentation threshold was reached. The material division threshold for the slope material was 50. A gray value greater than 50 represented soil, and a value less than 50 indicated fractures. In the initial state, the slope surface was relatively flat, with few fractures. At $t = 6$ h, fractures with small length and width as well as poor connectivity appeared at the bottom of the test area. As the rainfall experiment progressed, the fracture size gradually increased. At $t = 14$ h, the fractures developed to rills, and the number of rills increased significantly. At the end of the experiment, fractures and rills

were observed in the upper part of the test area. Much of the soil particle composition was lost, and the soil structure was destroyed.

To analyze temporal and spatial evolutionary processes of soil erosion, the test area was divided into three parts: parts A, B, and C. The rill density μ in each area was calculated using the following equation:

$$\mu = \frac{\sum_{i=1}^{n} A_i}{A_0} \tag{4}$$

where A_i is the area of each rill on the slope surface and A_0 is the total area of the slope surface. The temporal evolution process and spatial characteristics of soil erosion on the slope surface are shown in Fig. 12. With an increase in rainfall duration, a creep-type growth trend of rill density on the slope surface is observed. When the rainfall duration reaches

Fig. 8 Resistivity profile of Line 2 for different rainfall durations. **a** $t = 0$; **b** $t = 6$ h; **c** $t = 8$ h; **d** $t = 10$ h; **e** $t = 12$ h; **f** $t = 16$ h
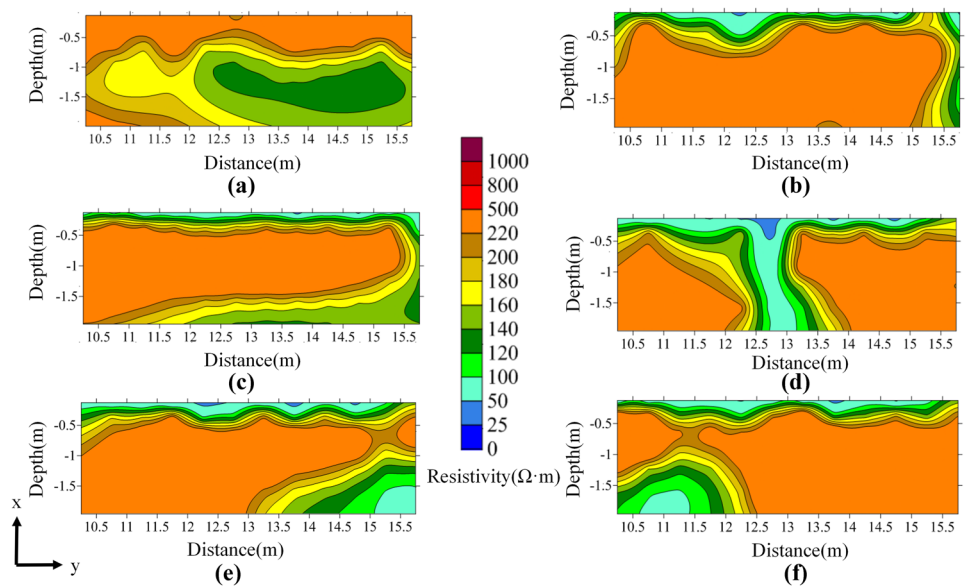
Fig. 9 Layered analysis of resistivity along slope depth with different rainfall durations (line 2)
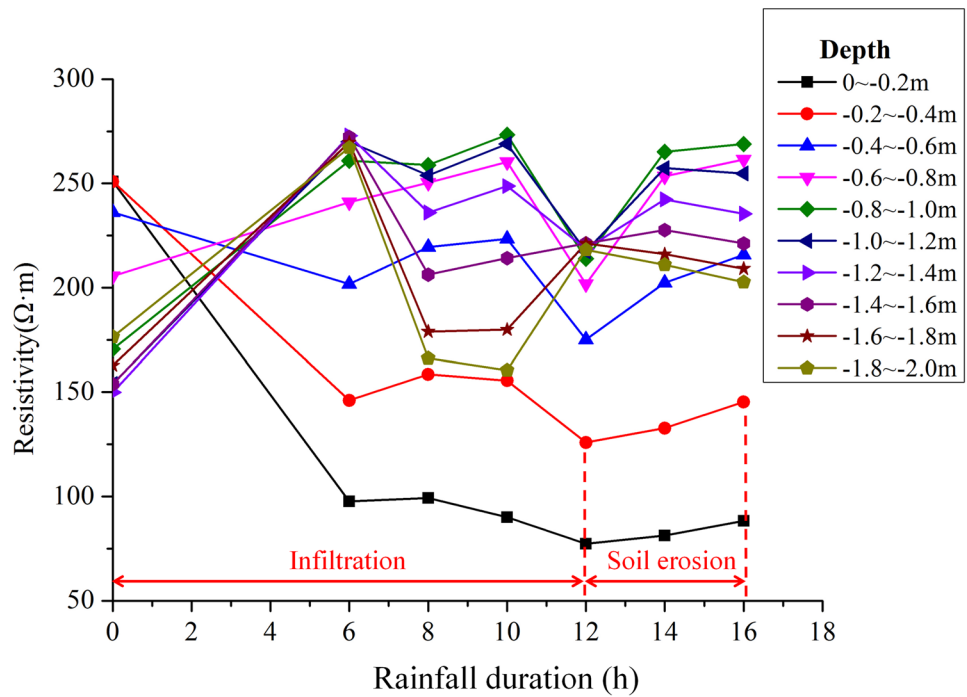
6 h, the rill density in parts A, B, and C is 0.6, 0.5, and 3.8, respectively, and the slope is still in the infiltration stage with overland flow. When the rainfall duration is 6–12 h, rill development is concentrated mainly in part C; furthermore, the rill density increases to 4.5%, and soil enters the initial erosion state with a small amount of sediment effluent. The

Fig. 10 Temporal and spatial variation in resistivity for different rainfall durations. **a** Line 2. **b** Line 1

(a)

(b)
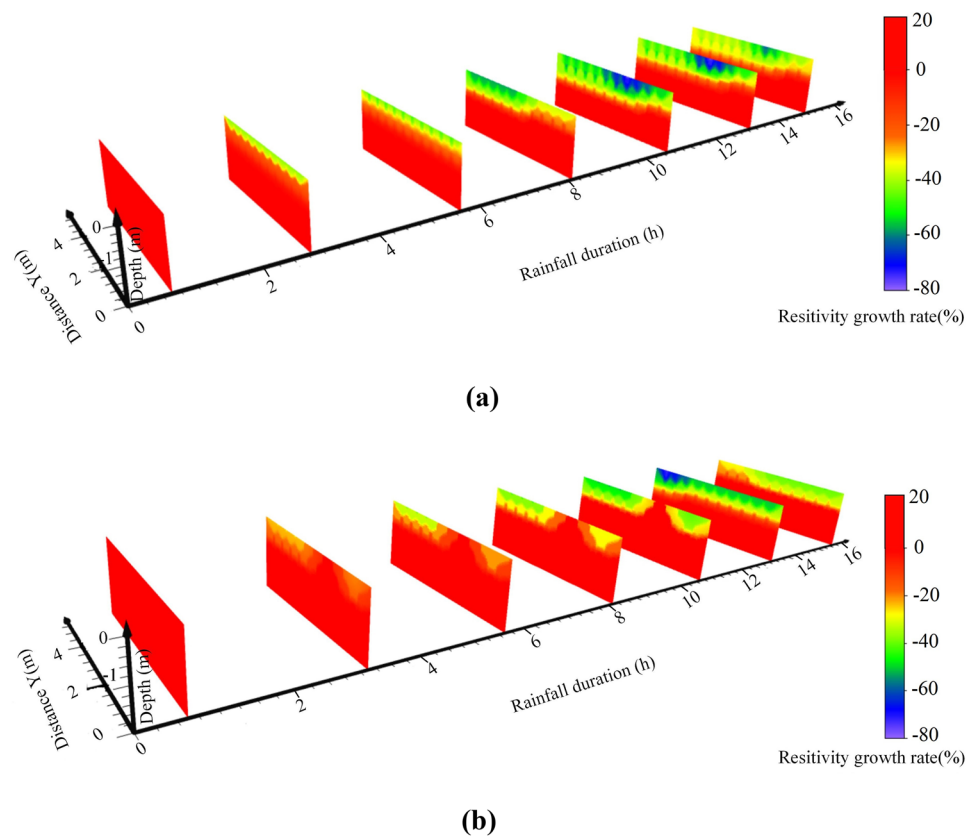
Fig. 11 Rill identification using the clustering method and rill distribution obtained for different rainfall duration. **a** $t = 0$; **b** $t = 6$ h; **c** $t = 10$ h; **d** $t = 12$ h; **e** $t = 14$ h; **f** $t = 16$ h
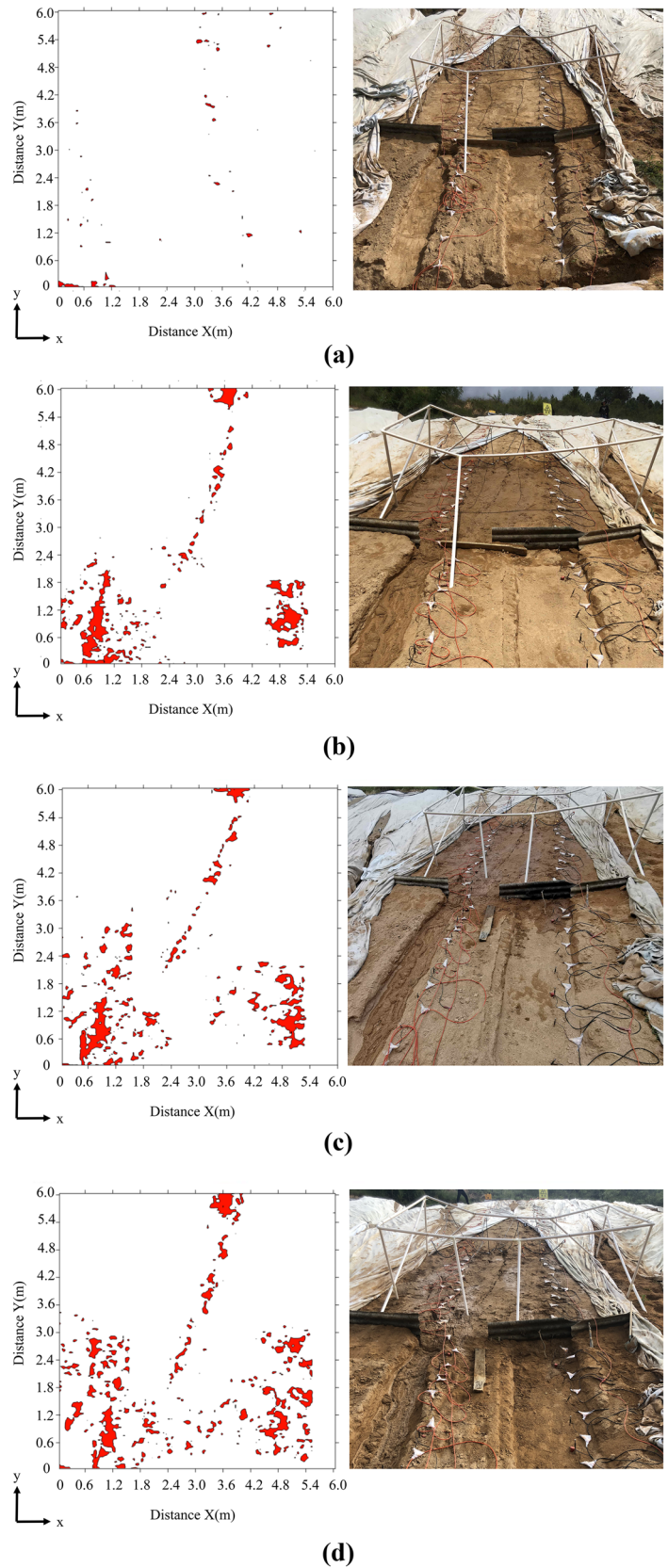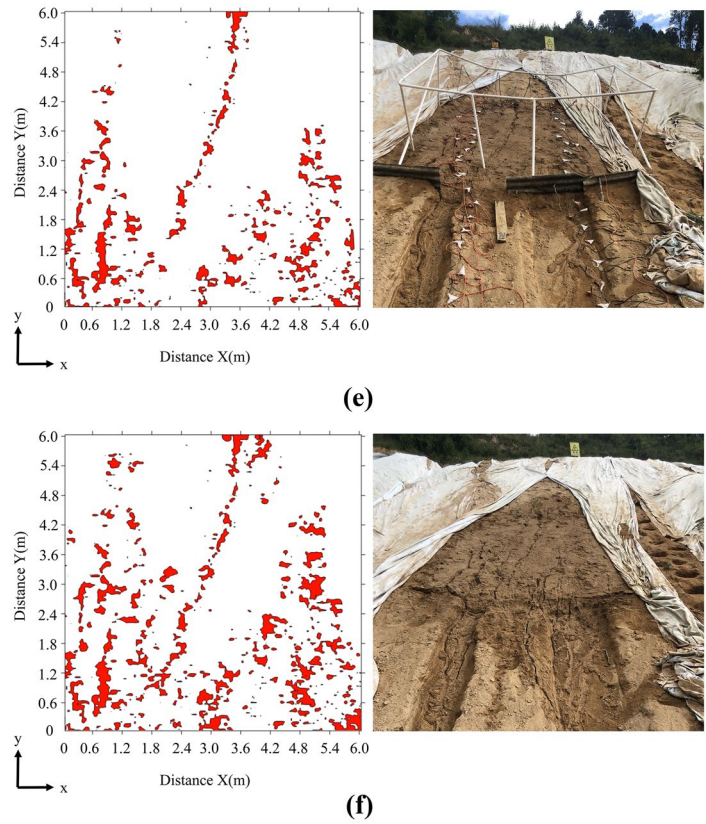

(a)

(b)

(c)

(d)

Fig. 11 (continued)

(e)

(f)

rill density in parts A and B is 0.8% and 2.3%, respectively. When the rainfall duration is 12–14 h, the soil erosion degree of the slope increases, and the rill density increases in parts A and B. The rill density in part C enters an accelerated erosion state with a large amount of sediment effluent. When the rainfall duration reaches 16 h, the rill densities in parts A, B, and C are 1.9%, 4.2%, and 7.3%, respectively. Generally, the rill density of part C is greatest on the slope surface.

Fig. 12 Temporal evolution process and spatial characteristics of rill density with different rainfall durations

a: Infiltration stage   b: Initial erosion stage   c: Accelerated erosion stage
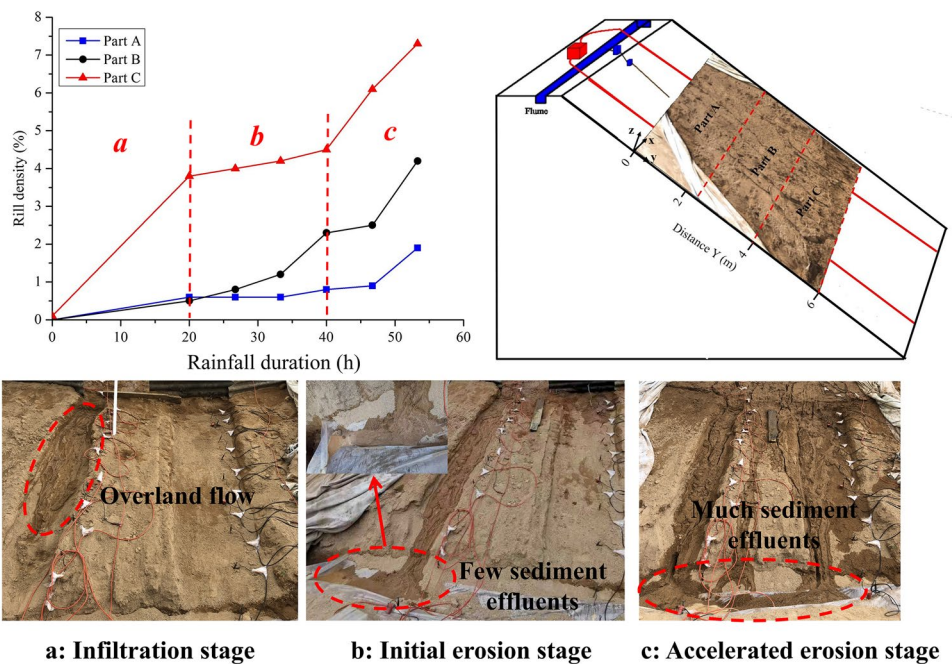
Spatio-temporal evolution laws of slope erosion due to rainfall

Correlation analysis of resistivity and soil erosion parameters

The soil erosion of a slope can be quantitatively evaluated from the rill density statistics using the volumetric method, as shown in Eq. (6) (Gilley et al. 1990; Zheng 1989). Temporal and spatial variations in resistivity can be determined using the resistivity growth rate calculated using Eq. (3). The moisture content of the soil increased in the early stage of the rainfall test ($t = 0–12$ h) due to infiltration. At the end of the rainfall test ($t = 12–16$ h), the moisture content of the soil in the shallow layer of the slope was generally saturated, and the soil erosion entered the differentiation stage. The change in moisture content during infiltration was much smaller than the change in resistivity due to soil erosion. At this stage, the resistivity change rate $\Delta\rho$ between different states is reflected as the change in soil structure caused by erosion, without considering the influence of moisture. The resistivity change rate $\Delta\rho$ and soil erosion rate ΔW_S are introduced to evaluate the effect of electrical application on soil erosion:

$$\Delta\rho = \frac{\rho_{n+1} - \rho_n}{\rho_n} \tag{5}$$

$$\begin{cases} W_n = \gamma_d \cdot \sum_{i=1}^{x} \left(\sum_{i=1}^{y} R_{Wi} \cdot R_{Hi} \right) \cdot R_L \Big/ y \\ \Delta W_s = \frac{W_{n+1} - W_n}{W_n} \end{cases} \tag{6}$$

where γ_d is the dry unit weight of soil; R_{Wi} is the rill width measured for the ith time; R_{Hi} is the rill depth measured for the ith time; R_L is the rill length; x is the total number of rills; y is the number of measurements per rill; n is the number of states, $t = 2n$; ρ_n is the resistivity when $t = 2n$; ρ_{n+1} is the resistivity when $t = 2(n + 1)$; W_n is the amount of soil erosion when $t = 2n$; W_{n+1} is the amount of soil erosion when $t = 2(n + 1)$; ρ_0 is the resistivity in the initial state; and ρ_1 is the resistivity when $t = 2$ h. The relationship between changes in the electrical parameters and soil erosion parameters was established by combining the electrical measurement test equations as follows:

$$\Delta W_s = a \cdot ln(\Delta\rho + 1) \tag{7}$$

where a is a coefficient related to the soil properties and other factors. In this experiment, a was 16.58. The soil erosion of the entire slope can be reflected by its change in resistivity. ΔW_S was measured for the entire slope, and the average resistivity of the entire slope was used to calculate the resistivity change rate, which can be used in Eq. (7). A logarithmic correlation exists between the resistivity change rate and the soil erosion change rate, as shown in Fig. 13. The correlation coefficient R^2 is 0.98. The results indicate that the equation has a high goodness of fit. The probability of the significance test with the regression equation is 0 (< 0.05).

Previous research indicates an exponential relationship between erosion and rainfall duration for the entire slope (Song et al. 2004). The relationship between soil erosion rate ΔW_S, rainfall duration t, and rainfall intensity I at different depths was established as follows:

$$\Delta W_s = a \cdot \left(1 - e^{b \cdot t \cdot I} \right) \tag{8}$$

where a and b are coefficients related to the soil properties and other factors; $I = 3.3$ mm/h in the test. Between 0 to -0.2 m and -0.2 to -0.4 m, a had values of -14.62 and -3.44, respectively, and b was 0.024 and 0.048, respectively. For line 2, the soil erosion rate was calculated using the measured resistivity profile data at the end of the rainfall test ($t = 12–16$ h), based on the relationship between electrical parameters and soil erosion parameters, as shown in Fig. 14. From 0 to -0.2 m, the soil erosion rate increased with increasing precipitation. Furthermore, the average soil erosion rate was 31% and 39% when the precipitation was 46.7 mm and 53.3 mm, respectively. From -0.2 to -0.4 m, the soil erosion rate increased with increasing precipitation. Moreover, the average soil erosion rate was 29% and 40% when the precipitation was 46.7 mm and 53.3 mm, respectively.

Spatio-temporal evolution laws of infiltration

The conductivity of a soil (σ) is related to the movement of ions and electrons and can be expressed by the Nernst–Einstein equation:
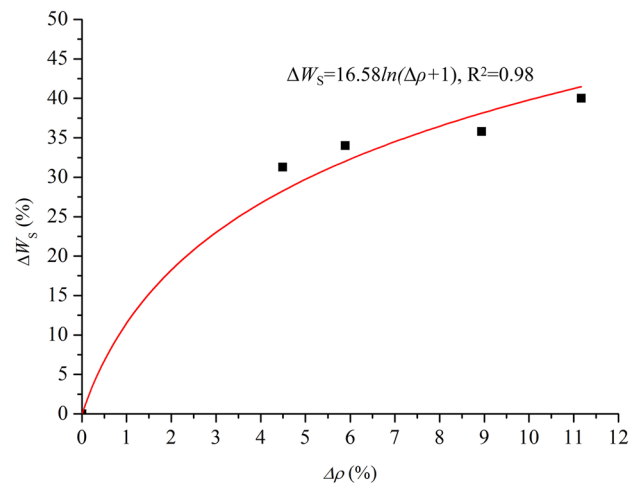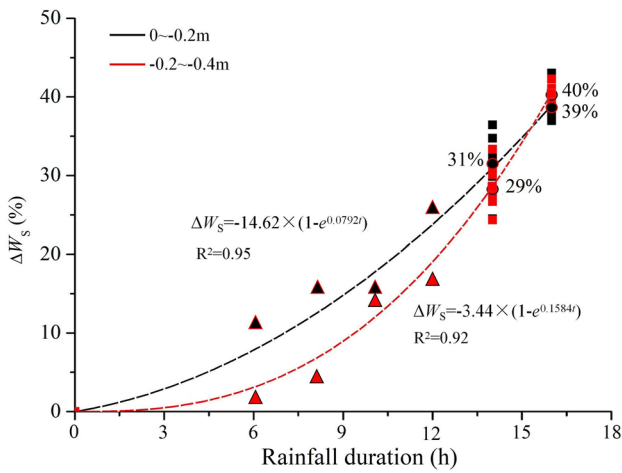

Fig. 13 Relationship between soil erosion and resistivity changes

Fig. 14 Relationship between soil erosion and rainfall duration determined by nonlinear fitting method

$$\sigma = \frac{n_i Z^2 e^2}{KT} D \qquad (9)$$

where n_i is the number of ion units; Z is the ion valence; e is the electronic charge; K is the Boltzmann's constant; T is the absolute temperature; and D is the diffusion coefficient (Gottlieb and Sollner 1968). The number of ion units n_i increases with the influence of infiltration, resulting in an increase in soil conductivity and a decrease in resistivity. The number of ion units n_i decreases with the influence of soil erosion, resulting in a decrease in soil conductivity and an increase in resistivity. For the soil conductivity model, changes in moisture content and loss of mineral components, expressed as $\Delta\sigma_\omega$ and $\Delta\sigma_W$, affect the ion concentration independently, leading to a change in soil conductivity. The model can be considered as a linear or approximately linear system. Based on the conductive mechanism of soil indicated in Eq. (9), the change in resistivity consists of two parts:

$$\Delta\rho = \Delta\rho_\omega + \Delta\rho_W \qquad (10)$$

where $\Delta\rho$ is the resistivity change rate; $\Delta\rho_\omega$ is the resistivity change rate due to moisture content; and $\Delta\rho_W$ is the resistivity
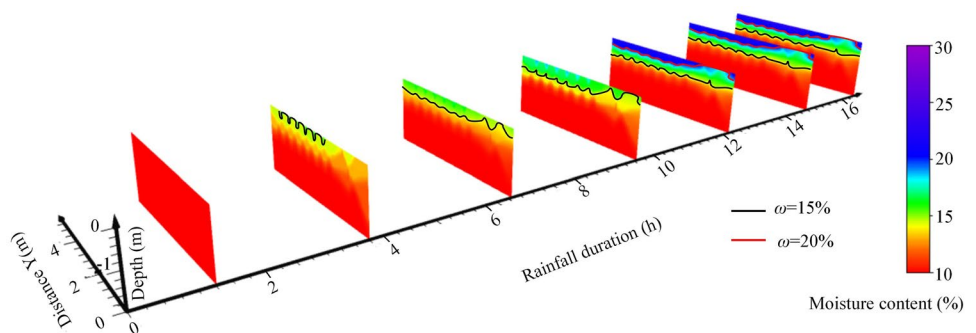
change rate due to soil erosion. Based on the existing soil resistivity–moisture content model and the distribution of the soil erosion change rate for different rainfall durations, the resistivity change rate due to moisture content $\Delta\rho_\omega$ was calculated. The moisture content ω in each state was calculated using the following equation:

$$\Delta\rho_\omega = e^{c*(\omega_{n+1}-\omega_n)} - 1 \qquad (11)$$

where c is a coefficient related to the soil properties and other factors; $b = -2.77$ in this experiment; n is the number of states; ω_n is the moisture content of the soil when $t = 2n$; and ω_{n+1} is the moisture content of the soil when $t = 2(n + 1)$. The temporal and spatial evolutionary processes of infiltration are shown in Fig. 15. In the initial state, the moisture content of the slope was approximately 10%. During rainfall, the moisture content gradually increased. When the rainfall duration was 4 h, the moisture content was between 10 and 15%, and the infiltration depth was approximately −0.2 to −0.4 m. When the rainfall duration was 10 h, the moisture content was between 13 and 20%, and the infiltration depth was approximately −0.2 to −0.4 m. The moisture content at the top of the slope was between 13 and 15%, and that at the bottom was between 15 and 20%. When the rainfall duration was 12 h, the moisture content was between 15 and 25%, and the infiltration depth was approximately −0.4 to −0.6 m. The moisture content at the top of the slope was between 15 and 20%, and that at the bottom of the slope was between 15 and 25%. The rainfall infiltration occurred in the slope depth and slope bottom directions.

Spatio-temporal evolution laws of soil erosion

The temporal and spatial evolutionary processes of soil erosion are shown in Fig. 16. In the initial state, the erosion rate ΔW_S of the slope was 0. During rainfall, the erosion rate gradually increased. When the rainfall duration was 8 h, the erosion rate was between 5 and 11%, and the erosion depth was approximately −0.2 to −0.4 m. When the rainfall duration was 12 h, the erosion rate was between 5 and 20%, and the erosion depth was approximately −0.2 to −0.4 m. The erosion

Fig. 15 Temporal and spatial evolutionary processes of moisture content considering infiltration

Fig. 16 Temporal and spatial evolutionary processes of erosion rate
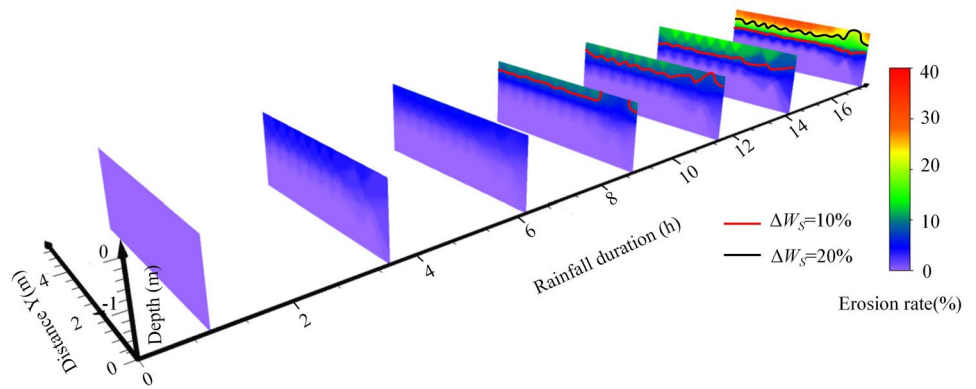
rate at the top of the slope was between 5 and 12%, and that at the bottom of the slope was between 5 and 15%. When the rainfall duration was 16 h, the erosion rate was between 5 and 40%, and the erosion depth was approximately −0.4 to −0.6 m. The erosion rate at the top of the slope was between 5 and 25%; the erosion rate at the bottom of the slope was between 5 and 40%. Influenced by the particle migration path, the erosion degree was significant on the slope surface and at the slope bottom.

Based on the evolutionary process and spatial difference in slope erosion, the spatial sequence of each period was decomposed into a low-frequency trend term,

a high-frequency periodic term, and an irregular residual term by the seasonal and trend decomposition using loess (STL) method:

$$Y = T + S + R \tag{12}$$

where Y is the observed data; T is the trend component; S is the seasonal component; and R is the remainder component (Koc et al. 2000). The trend component T is the resistivity response under the influence of infiltration and soil erosion. The seasonal component S and remainder component R are the resistivity response under the influence of rainfall on the electrodes and complex movement of moisture and

**Fig. 17** Step-type evolution of slope erosion using STL
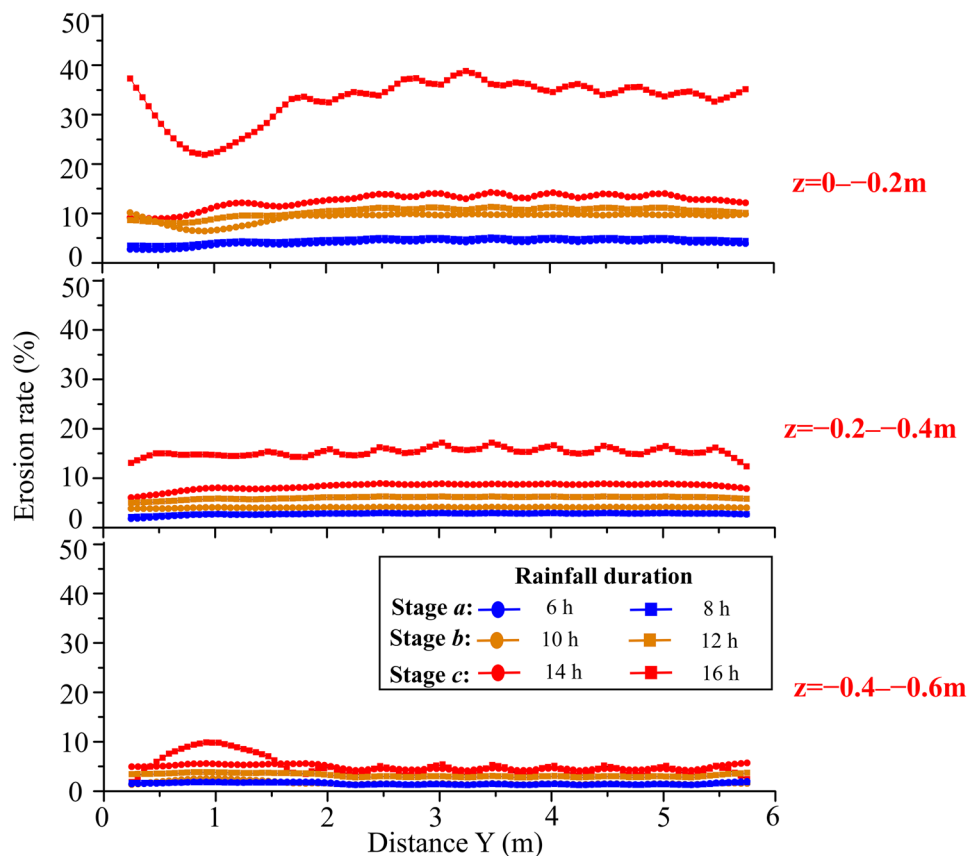
Fig. 18 Spatial characteristics of slope erosion with rainfall duration of 16 h
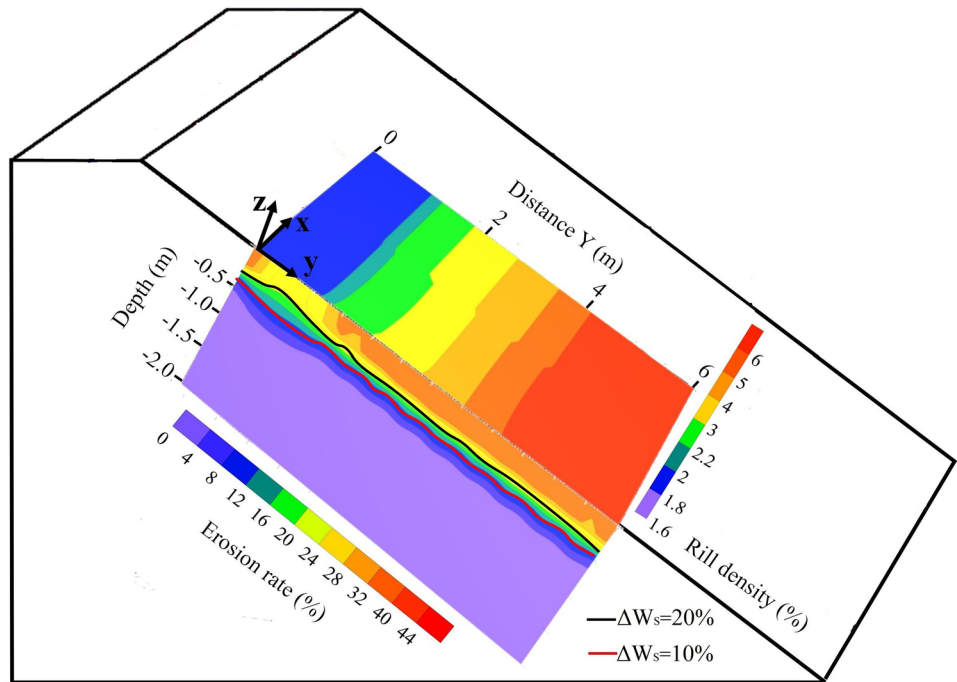
particles. Detrending and deseasonalizing were conducted to decompose the spatial resistivity of each period Y; the trend component T and seasonal component S were obtained using low-pass filtering and smoothing to remove interference (Cleveland et al. 1990). Calculating the spatial trend of slope erosion in each state, a temporal and spatial evolution process of slope erosion was observed along the slope depth, as shown in Fig. 17. With an increase in rainfall duration, a step-type growth trend for erosion rate was observed along the slope depth. When the rainfall duration was less than 6 h (infiltration stage), the erosion rate was relatively stable at each depth, When the rainfall duration was 6–12 h (initial erosion stage), the erosion rate ranged from 8.0 to 11.3% at a depth of 0 to −0.2 m. At a depth of −0.2 to −0.4 m, the erosion rate ranged from 4.9 to 6.2%; furthermore, at a depth of −0.4 to −0.6 m, the erosion rate ranged from 2.7 to 3.8%. The average growth rates were 10.3%, 6.0%, and 3.1%, respectively. With an increase in rainfall duration, the degree of erosion at a depth of 0 to −0.4 m rapidly increased. When the rainfall duration was 12–16 h (accelerated erosion stage), an obvious step-type growth trend was observed for the erosion rate in the area ($z = 0$ to −0.4 m, $y = 2$–6 m); the erosion rate was 21.8–38.8% at a depth of 0 to −0.2 m. At a depth of −0.2 to −0.4 m, the erosion rate was 12.3–17.2%. Furthermore, at a depth of −0.4 to −0.6 m, the erosion rate ranged from 1.8 to 9.8%. The average growth rates were 33.0%, 15.2%, and 4.9%.

The slope erosion characteristic is shown in Fig. 18. There are great differences in soil erosion at different depths of the slope. The erosion degree in the area ($z = 0$ to −0.2 m, $y = 2$–6 m) is the largest and causes local collapse. Due to the depth of erosion, ordinary vegetation is less effective protection. With increases in rainfall duration, the degree of erosion at a given depth increases sharply. Many soil particles are lost, and less vegetation can survive erosion, eventually leading to a decrease in soil strength in the slope depth, slope instability, and local collapse.
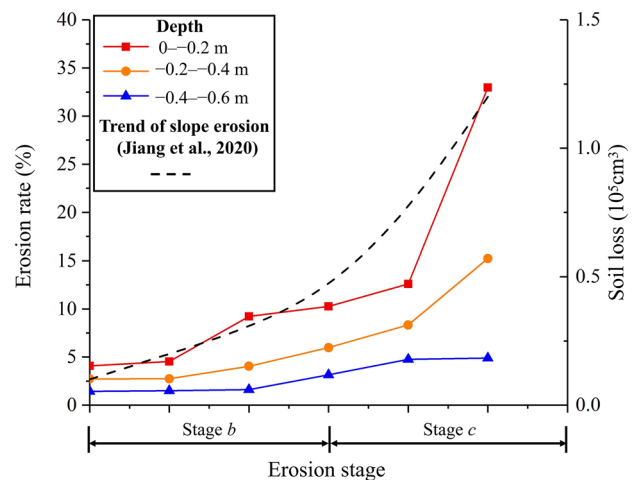
Fig. 19 Slope erosion trend along slope depth with increase in rainfall duration

Fig. 20 Erosion stage monitoring of highway slope after several monsoons

Slope excavation → One monsoon → Two monsoons
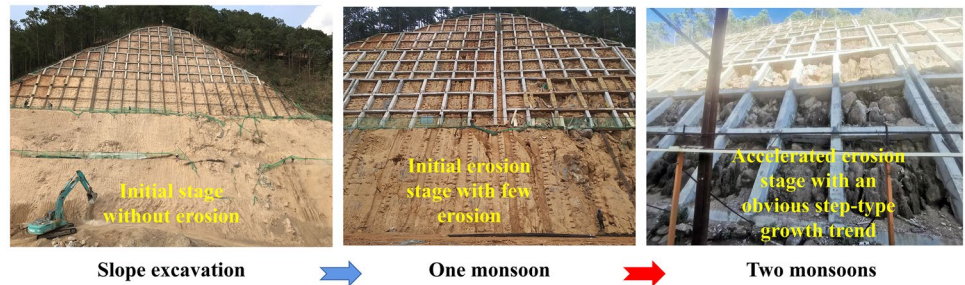
Discussion

Processes and characteristics of slope erosion

Owing to a lack of research on the erosional characteristics of slopes along the depth direction, evolution laws for slope erosion due to rainfall were analyzed, and spatio-temporal characteristics of slope erosion were obtained through electrical measurements. According to previous studies, the process of rainfall erosion can be divided into a short initial stage (infiltration, no erosion, or splash erosion), sheet flow and rill development stages (initial erosion), and a rill stable stage (accelerated erosion) (Rahardjo et al. 2010; Quan et al. 2020; Wu et al. 2020). The temporal evolution of slope erosion is shown in Figs. 17 and 19. A theoretical basis for the early warning of slope instability from erosion could be achieved. A step-type growth trend for erosion rate from 8.0–11.3% (infiltration and initial erosion) to 21.8–38.8% (accelerated erosion) was observed. These results are consistent with those of other researchers (Jiang et al. 2020). The evolution trend of erosion is similar at different depths, and the growth rate varies with depth. The erosion stage at greater depths lags behind the erosion stage at shallow depths.

Erosional characteristics of the slope were obtained, as shown in Fig. 18. For erosional characteristics down the slope, a high soil moisture content can lead to the formation of rill incision after the initial rainfall (Kuhn and Bryan 2004). The bottom location exhibits the maximum decrease rate, followed by the middle and the top locations for the angle slope due to the confluence of runoff and sediment from the top to the foot of the slope (Liu et al. 2020). In this study, the erosion at the bottom of the slope was the greatest, and caused local collapse. This result is consistent with that of previous research (Iverson and Major 1986). We determined the erosional characteristics along the slope depth. A gradual decreasing trend of erosion rate was observed from the shallow to the deep parts of the slope. When the rainfall duration was 16 h, the average erosion rates were 4.9%, 15.2%, and 33.0%. The results were verified by the rill characteristics on the surface. These results are important for erosion degree estimation, stability analysis, early warning, and prevention of slope instability.

Slope stability considering soil erosion

Field monitoring of erosion on a highway slope was performed to further verify and expand the obtained conclusions.

Fig. 21 Monitoring data analysis using cluster method to determine erosion stages
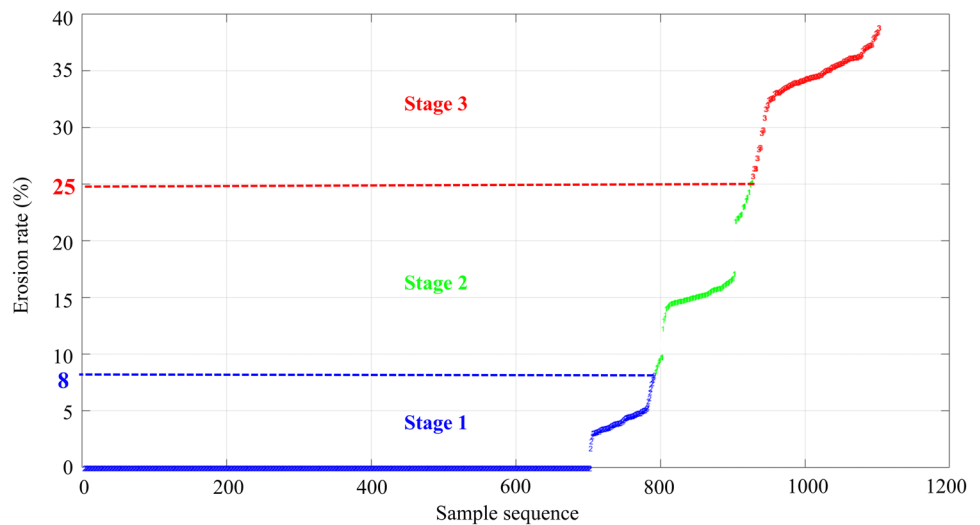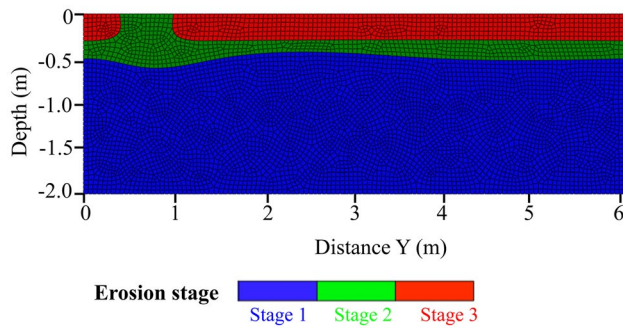
Fig. 22 Mesh profile of slope considering erosion stage for stability analysis

Completely decomposed granite was exposed to the environment after the excavation without erosion. In the initial erosion stage after one monsoon, few cracks appeared on the slope. Many cracks formed and local collapse occurred after two monsoons, reflecting an obvious step-type growth trend, as shown in Fig. 20. The matrix suction and shear strength of slope soil decrease under the influence of rainfall; furthermore, fine particles are removed from the slope due to seepage, leading to shallow landslides (Zhang et al. 2011; Crosta and Prisco 1999). Generally, the erosional characteristics of slopes in the depth direction are necessary for monitoring and early warning.

To analyze slope stability with soil erosion, the erosion stages were determined using cluster analysis for different erosion rates, as shown in Fig. 21. The stage thresholds were determined through the clustering method. Three erosion states were defined: stage 1, stage 2, and stage 3. The mesh profile was obtained from the slope erosion characteristics, as shown in Fig. 18, and erosion stage thresholds, as shown in Fig. 22. Different erosion stages correspond to different soil parameter constitutive models. Based on the erosion stage, slope stability with soil erosion can be further analyzed. Considering the soil erosion constitutive model (Cividini and Gioda 2004) and hydraulic characteristic equation (Mualem 1976; Carman 1939), the position of the sliding surface is assumed. The slope stability safety factor is calculated using the infinite slope stability analysis method and the finite element calculation method, and the soil erosion is considered in the analysis (Zhang et al. 2019).

Conclusions

To enable continuous detection in the depth direction, electrical measurements and 3D laser scanning were used to determine the spatio-temporal evolution laws and characteristics of soil erosion on a completely decomposed granite slope due to rainfall. The following conclusions can be drawn from the in situ model tests:

1. Temporal and spatial variations in resistivity can be determined. Resistivity exhibits a decreasing trend with increasing moisture content, while soil erosion effect is low. With an increase in precipitation, shallow surface soil exhibits saturation, and resistivity exhibits an increasing trend with increasing degree of soil erosion due to particle migration.

2. Slope surface shape parameters such as rill rate and width were calculated using the volumetric method in different precipitation conditions. Generally, the rill density at the bottom is greater, and rill develops first at the bottom of the slope and gradually extends to the top of the slope. With an increase in rainfall duration, a creep-type growth trend of rill density on the slope surface is observed, with rill density change rates of approximately 0.6%/h, 0.1%/h, and 0.7%/h.

3. The effect of moisture on resistivity was removed based on Nernst–Einstein equation; spatio-temporal characteristics of slope erosion and relationships between resistivity, precipitation, and erosion parameters were determined using the nonlinear fitting method. A step-type growth trend of the erosion rate, from 8.0–11.3% (stage *a* and stage *b*: infiltration and initial erosion) to 21.8–38.8% (stage *c*: accelerated erosion), was observed. A gradual decreasing trend of erosion rate was observed from the shallow to deep parts of the slope. When the rainfall duration was 16 h, the average erosion rates were 33.0%, 15.2%, and 4.9%. The results provide a basis for determining the degree of erosion and analyzing the stability of field slopes.

Data availability Some or all data, models, or code generated or used during the study are available from the corresponding author by request.

References

Acharya G, Cochrane T, Davies T, Bowman E (2011) Quantifying and modeling post-failure sediment yields from laboratory-scale soil erosion and shallow landslide experiments with silty loess. Geomorphology 129(1–2):49–58

Ahmad N (2018) Detection of subsurface cracking depth using electrical resistivity tomography: a case study in Masjed-Soleiman, Iran. Constr Build Mater 192:1103–1108

Ayodele AL, Pamukcu S, Shrestha RA, Agbede OA (2017) Electrochemical soil stabilization and verification. Geotech Geol Eng 36:1283–1293

Biali G, Patriche CV, Pavel VL (2014) Application of GIS techniques for the quantification of land degradation caused by water erosion. Environ Eng Manag J 13(10):2665–2673

Biswas A, Roy P (2018) Meso-scale flanking structure and microscale push up structure within migmatitic biotite granite, Peninsular Gneissic Complex, Southern India. Int J Earth Sci 107(1):167–168

Cai GH, Du YJ, Liu SY, Singh DN (2015) Physical properties electrical resistivity and strength characteristics of carbonated silty soil admixed with reactive magnesia. Can Geotech J 52(11):1699–1713

Cano-Paoli K, Chiogna G, Bellin A (2019) Convenient use of electrical conductivity measurements to investigate hydrological processes in Alpine headwaters. Sci Total Environ 685:37–49

Carman PC (1939) Permeability of saturated sands, soils and clays. J Agric Sci 29(2):262–273

Chehlafi A, Kchikach A, Derradji A, Mequedade N (2019) Highway cutting slopes with high rainfall erosion in Morocco: evaluation of soil losses and erosion control using concrete arches. Eng Geol 260:105200

Chen H, Lee C, Law K (2004) Causative mechanisms of rainfall-induced fill slope failures. J Geotech Geoenviron Eng 130(6):593–602

Cividini A, Gioda G (2004) Finite-element approach to the erosion and transport of fine particles in granular soils. Int J Geomech 4(3):191–198

Cleveland RB, Cleveland WS, McRae JE, Terpenning I (1990) STL: a seasonal-trend decomposition. J off Stat 6(1):3–73

Comino JR, Senciales JM, Ramos MC, Martínez-Casasnovas JA, Lasanta T, Brevik EC, Ries JB, Ruiz Sinoga JD (2017) Understanding soil erosion processes in Mediterranean sloping vineyards (montes de málaga, spain). Geoderma 296:47–59

Crosta G, Prisco CD (1999) On slope instability induced by seepage erosion. Can Geotech J 36(6):1056–1073

Cui Y, Jiang Y, Guo C (2019) Investigation of the initiation of shallow failure in widely graded loose soil slopes considering interstitial flow and surface runoff. Landslides 16(4):815–828

Fang LL, Qi JL, Ma W (2012) Freeze-thaw induced changes in soil structure and its relationship with variations in strength. J Glaciol Geocryol 2:435–440

Forster GR, Meyer LD (1972) Transport of soil particles by shallow flow. Trans Am Soc Agric Eng 15(1):99–102

Gilley JE, Kottwitz ER, Simanton JR (1990) Hydraulic characteristics of rills. Trans ASAE 33(6):1900–1906

Gottlieb MH, Sollner K (1968) Failure of the Nernst-Einstein equation to correlate electrical resistances and rates of ionic self-exchange across certain fixed charge membranes. Biophys J 8(5):515–535

Grigor'ev VY, Kuznetsov MS, Abdulkhanova DR, Bazarov OA (2008) Calculation of parameters of soil particles detached and transported by shallow flows upon rill erosion. Eurasian Soil Sci 41(3):302–311

Hama NA, Ouahbi T, Taibi S, Souli H, Fleureau JM, Pantet A (2017) Relationships between the internal erosion parameters and the mechanical properties of granular materials. Eur J Environ Civ Eng 23(11):1368–1380

Hicher PY (2013) Modelling the impact of particle removal on granular material behaviour. Géotechnique 63(2):118–128

Iverson RM, Major JJ (1986) Groundwater seepage vectors and the potential for hillslope failure and debris flow mobilization. Water Resour Res 22(11):1543–1548

Jiang YM, Shi HJ, Wen ZM, Guo MH, Zhao J, Cao XP, Fan YM, Zheng C (2020) The dynamic process of slope rill erosion analyzed with a digital close range photogrammetry observation system under laboratory conditions. Geomorphology 350:106893

Karim MZ, Tucker-Kulesza SE (2018) Predicting soil erodibility using electrical resistivity tomography. J Geotech Geoenviron Eng 144(4):1–11

Kibria G (2014) Evaluation of physico-mechanical properties of clayey soils using electrical resistivity imaging technique. The University of Texas at Arlington, USA (PhD thesis)

Kim YK, Lee RR (2010) Field infiltration characteristics of natural rainfall in compacted roadside slopes. J Geotech Geoenviron Eng 136(1):248–252

Koc B, Ma Y, Lee Y (2000) Smoothing STL files by Max-Fit biarc curves for rapid prototyping. Rapid Prototyp J 6(3):186–205

Kuhn NJ, Bryan RB (2004) Drying, soil surface condition and interrill erosion on two ontario soils. CATENA 57(2):113–133

Léonard J, Richard G (2004) Estimation of runoff critical shear stress for soil erosion from soil shear strength. CATENA 57(3):233–249

Liu WP, Ouyang GQ, Luo XY, Luo J, Hu LN, Fu MF (2020) Moisture content, pore-water pressure and wetting front in granite residual soil during collapsing erosion with varying slope angle. Geomorphology 362:107210

Liu Z, Zhu SJ, Shi HG, Wang YH, Tong N, Chen JX (2014) Discussion on integrated management technology of mapping data for Highway One in Congo (Brazzaville). Sci Surv Mapp 39(11):126–128

Masrur M, Bora M, Kristen SC (2019) Freeze-thaw performance of phase change material (PCM) incorporated pavement subgrade soil. Constr Build Mater 202:449–464

Mualem Y (1976) A new model for predicting the hydraulic conductivity of unsaturated porous media. Water Resour Res 12(3):513–522

Pizer SM, Amburn EP, Austin JD (1987) Adaptive histogram equalization and its variations. Comput vis Graph Image Process 39(3):355–368

Quan X, He J, Cai Q, Sun L, Wang S (2020) Soil erosion and deposition characteristics of slope surfaces for two loess soils using indoor simulated rainfall experiment. Soil till Res 204:104714

Rahardjo H, Ong TH, Rezaur RB, Leong EC, Fredlund DG (2010) Response parameters for characterization of infiltration. Environ Earth Sci 60(7):1369–1380

Song W, Liu PL, Yang MY (2004) Study on erosion process by the REE tracer method. Adv Water Sci 15(2):197–201

Wang YC, Lai CC (2018) Evaluating the erosion process from a single-stripe laser-scanned topography: a laboratory case study. Water 10(7):956

Wen X, Deng X (2020) Current soil erosion assessment in the Loess Plateau of China: a mini-review. J Clean Prod 276(3):123091

Wu Q, Wang CM, Song PR, Zhu HB, Ma DH (2014) Rainfall scouring test and 3D particle flow fluid solid coupling simulation of loess steep slope. Rock Soil Mech 4:977–985

Wu SB, Chen L, Wang NL, Li J, Li JK (2020) Two-dimensional rainfall-runoff and soil erosion model on an irregularly rilled hillslope. J Hydrol 580:124346

Yu Y, Wei W, Chen LD, Feng TJ, Daryanto S (2019) Quantifying the effects of precipitation, vegetation, and land preparation techniques on runoff and soil erosion in a Loess watershed of China. Sci Total Environ 652:755–764

Zhang L, Wu F, Zhang H, Zhang L, Zhang J (2019) Influences of internal erosion on infiltration and slope stability. Bull Eng Geol Env 78(3):1815–1827

Zhang LL, Zhang J, Zhang LM, Tang WH (2011) Stability analysis of rainfall-induced slope failure: a review. Proc Inst Civ Eng Geotech Eng 164(5):299–316

Zheng FL (1989) A research on method of measuring rill erosion amount. Bull Soil Water Conserv 4:41–45